How to cite: *Angew. Chem. Int. Ed.* **2024**, *63*, e202408574
doi.org/10.1002/anie.202408574

Superionic Conductors

Superionic Conduction in K_3SbS_4 Enabled by Cl-Modified Anion Lattice

*Yudan Chen[+], Pengbo Wang[+], Erica Truong, Bright Ogbolu, Yongkang Jin, Ifeoluwa Oyekunle, Haoyu Liu, M. Mahinur Islam, Tej Poudel, Chen Huang, Ivan Hung, Zhehong Gan, and Yan-Yan Hu**

Abstract: All-solid-state potassium batteries emerge as promising alternatives to lithium batteries, leveraging their high natural abundance and cost-effectiveness. Developing potassium solid electrolytes (SEs) with high room-temperature ionic conductivity is critical for realizing efficient potassium batteries. In this study, we present the synthesis of $K_{2.98}Sb_{0.91}S_{3.53}Cl_{0.47}$, showcasing a room-temperature ionic conductivity of 0.32 mS/cm and a low activation energy of 0.26 eV. This represents an increase of over two orders of magnitude compared to the parent compound K_3SbS_4, marking the highest reported ionic conductivity for non-oxide potassium SEs. Solid-state ^{39}K magic-angle-spinning nuclear magnetic resonance on $K_{2.98}Sb_{0.91}S_{3.53}Cl_{0.47}$ reveals an increased population of mobile K^+ ions with fast dynamics. Ab initio molecular dynamics (AIMD) simulations further confirm a delocalized K^+ density and significantly enhanced K^+ diffusion. This work demonstrates diversification of the anion sublattice as an effective approach to enhance ion transport and highlights $K_{2.98}Sb_{0.91}S_{3.53}Cl_{0.47}$ as a promising SE for all-solid-state potassium batteries.

Introduction

All-solid-state batteries (ASSBs) have emerged as the next-generation electrochemical energy storage devices due to their enhanced safety and higher energy density.[1–5] Solid electrolytes (SEs) with high ionic conductivity are crucial for the cyclability and overall efficiency of ASSBs. Up to the present, lithium SEs have been extensively studied and well-developed. Oxides, such as cation-doped $Li_7La_3Zr_2O_{12}$, can exhibit an ionic conductivity over 1 mS/cm at room temperature, along with a wide electrochemical stability window and robust chemical stability.[6–8] Sulfide SEs, like mixed-halide argyrodites, can achieve ionic conductivity values over 25 mS/cm, exceeding those of liquid electrolytes.[9–12] However, limitations in lithium availability are steering attention towards abundantly available alternative energy storage systems, with a particular emphasis on sodium and potassium.[13–19]

Sodium SEs have gained significant attention and advancement in the past decade. Materials such as Ca-doped Na_3PS_4 have demonstrated remarkable ionic conductivity, surpassing 1 mS/cm at room temperature.[20] An analog of Na_3PS_4, Na_3SbS_4, exhibits an impressive ionic conductivity of 3 mS/cm.[21] Through W doping in Na_3SbS_4, the ionic conductivity can be elevated to 32 mS/cm,[22] surpassing the performance of all lithium SEs.

In contrast, research on potassium SEs is still in the early stages. Only limited solid-state K-ion conductors, primarily oxide-based materials, have exhibited favorable ionic conductivities. However, these materials achieve practical conductivities, i.e., >0.1 mS/cm, only at elevated temperatures exceeding 300 °C.[23–26] Apart from oxides, Johrendt et al. discovered a potassium phosphidosilicate electrolyte, KSi_2P_3, demonstrating a bulk ionic conductivity of 0.26 mS/cm at room temperature with an activation energy of 0.20 eV.[27] More recently, inspired by the work in W-doped Na_3SbS_4, Wu et al. reported the first sulfide-based potassium SE, $K_{2.92}Sb_{0.92}W_{0.08}S_4$, attaining a bulk ionic conductivity of 0.14 mS/cm at 40 °C with an activation energy of 0.27 eV.[28]

Anion doping is an effective strategy to induce structural disorder for enhancing ion mobility and achieving synergies of various classes of materials.[11,29–33] Cl is often chosen in anion doping due to the abundant availability and cost-effectiveness of its precursor, which are crucial for facilitating large-scale production. In this study, we synthesized Cl-doped K_3SbS_4. An ionic conductivity of 0.32 mS/cm at 22 °C with an activation energy of 0.26 eV was achieved in $K_{2.98}Sb_{0.91}S_{3.53}Cl_{0.47}$. We employed ^{39}K solid-state nuclear magnetic resonance (NMR) in combination with ab initio molecular dynamic (AIMD) simulations to uncover the

[*] Y. Chen,[+] P. Wang,[+] E. Truong, B. Ogbolu, Y. Jin, I. Oyekunle, H. Liu, M. M. Islam, Prof. Y.-Y. Hu
Department of Chemistry and Biochemistry
Florida State University
Tallahassee, FL 32306 (USA)
E-mail: yhu@fsu.edu

I. Hung, Z. Gan, Prof. Y.-Y. Hu
Center of Interdisciplinary Magnetic Resonance
National High Magnetic Field Laboratory
Tallahassee, FL 32310 (USA)

T. Poudel, Prof. C. Huang, Prof. Y.-Y. Hu
Materials Science and Engineering
Florida State University
Tallahassee, FL 32310 (USA)

[+] These authors contributed equally to this work.

correlations between enhanced ionic conductivity and local site disorder induced via Cl-doping.

Results and Discussion

$K_{2.98}Sb_{0.91}S_{3.53}Cl_{0.47}$ was prepared via high-energy mechanochemical ball milling of K_2S, Sb_2S_3, S, and KCl (see Supporting Information for more details). The powder X-ray diffraction (PXRD) patterns of the as-synthesized K_3SbS_4 and $K_{2.98}Sb_{0.91}S_{3.53}Cl_{0.47}$, alongside β-$K_3SbS_4$ obtained from the Inorganic Crystal Structure Database (ICSD), are shown in Figure 1a. The parent compound β-K_3SbS_4 belongs to the $Cmc2_1$ space group and consists of four distorted SbS_4^{3-} tetrahedral units and two distinct potassium sites: K1 at the 8b site and K2 at the 4b site.[28,34] The PXRD pattern of the as-synthesized K_3SbS_4 exhibits broad peaks, indicating relatively low crystallinity. Conversely, Cl-doped $K_{2.98}Sb_{0.91}S_{3.53}Cl_{0.47}$ demonstrates higher crystallinity, with no observable additional peaks or apparent peak shifts in the PXRD patterns, compared to the β-K_3SbS_4 (ICSD). Figure 1b shows the PXRD Rietveld refinement of $K_{2.98}Sb_{0.91}S_{3.53}Cl_{0.47}$ (see Figure S1 for more details). The refinement result yields a low weighted profile R-factor (Rwp) of 4.65 % and a correspondingly low Goodness of Fit (GoF) value of 2.32, suggesting the high accuracy and reliability of the refined crystal structure.

Figure 1c displays the structure of $K_{2.98}Sb_{0.91}S_{3.53}Cl_{0.47}$ obtained from Rietveld refinement of the powder X-ray diffraction pattern. $K_{2.98}Sb_{0.91}S_{3.53}Cl_{0.47}$ maintains the primary $Cmc2_1$ structure. Like the parent compound K_3SbS_4, K^+ in the $K_{2.98}Sb_{0.91}S_{3.53}Cl_{0.47}$ occupies two Wyckoff positions: K1 at the 8b site and K2 at the 4b site. S^{2-} takes two Wyckoff positions: S1 and S3 at the 4a site and S2 at the 8b site. The refined unit cell parameters of $K_{2.98}Sb_{0.91}S_{3.53}Cl_{0.47}$ are summarized in Table S1. When Cl^- partially replaces S^{2-}, the unit cell volume of $K_{2.98}Sb_{0.91}S_{3.53}Cl_{0.47}$ ($a = 10.71210$ Å, $b = 11.27830$ Å, $c = 7.69884$ Å) experiences a slight reduction compared to the parent compound β-K_3SbS_4 ($a = 10.71200$ Å, $b = 11.28900$ Å, $c = 7.70520$ Å). Cl^- occupies 11.8 % of the S^{2-} sites, creating substantial site disorder. The Rietveld refinement shows a high phase purity with 98.3 % $K_{2.98}Sb_{0.91}S_{3.53}Cl_{0.47}$ and 1.7 % KCl. For the as-synthesized K_3SbS_4, the Rietveld refinement shows the coexistence of α-K_3SbS_4 and β-K_3SbS_4 in the sample, with a phase fraction of 33.3 % and 66.7 %, respectively (Figure S2, Table S2). Distinct from β-K_3SbS_4, α-K_3SbS_4 belongs to the $I\bar{4}3m$ space group and consists of only one K site at 6b and an ideal SbS_4^{3-} tetrahedral unit without distortion. The PXRD pattern of the empty sample holder with the Kapton polyimide film is also obtained to confirm that the two large bumps observed below $2\theta = 25°$ are from the background (Figure S3).

The ionic conductivity of $K_{2.98}Sb_{0.91}S_{3.53}Cl_{0.47}$ is determined using alternating current (AC) electrochemical impedance spectroscopy (EIS). Figure 2a shows the EIS Nyquist plot of $K_{2.98}Sb_{0.91}S_{3.53}Cl_{0.47}$ measured at 22 °C. The total ionic conductivity is calculated from the total resistance obtained from the equivalent circuit fitting of the Nyquist plot. The R1-CPE1 circuit is used to model the bulk and grain boundary contributions in the high-frequency region, and CPE2 is used to depict K^+ polarization at the blocking electrodes in the low-frequency region.[35] $K_{2.98}Sb_{0.91}S_{3.53}Cl_{0.47}$ exhibits an ionic conductivity of 0.32 mS/cm at room temperature. The electronic conductivity of $K_{2.98}Sb_{0.91}S_{3.53}Cl_{0.47}$ is determined to be 1.5×10^{-8} S/cm at 22 °C using the potentiostatic polarization method with indium foils as the ion-blocking electrodes (Figure 2b). The as-synthesized K_3SbS_4 has a total ionic conductivity of 4.2×10^{-4} mS/cm and an electronic conductivity of 8.3×10^{-10} S/cm at room temperature (Figure S4). Figure 2c exhibits the temperature dependence of the ionic conductivity of $K_{2.98}Sb_{0.91}S_{3.53}Cl_{0.47}$, which follows an Arrhenius behavior, $\sigma_{ion}T = \sigma_0 \exp(-E_a/k_BT)$, where σ_0 denotes the Arrhenius pre-exponential factor or pre-factor, E_a is the activation energy, k_B represents the Boltzmann constant, and T is the temper-

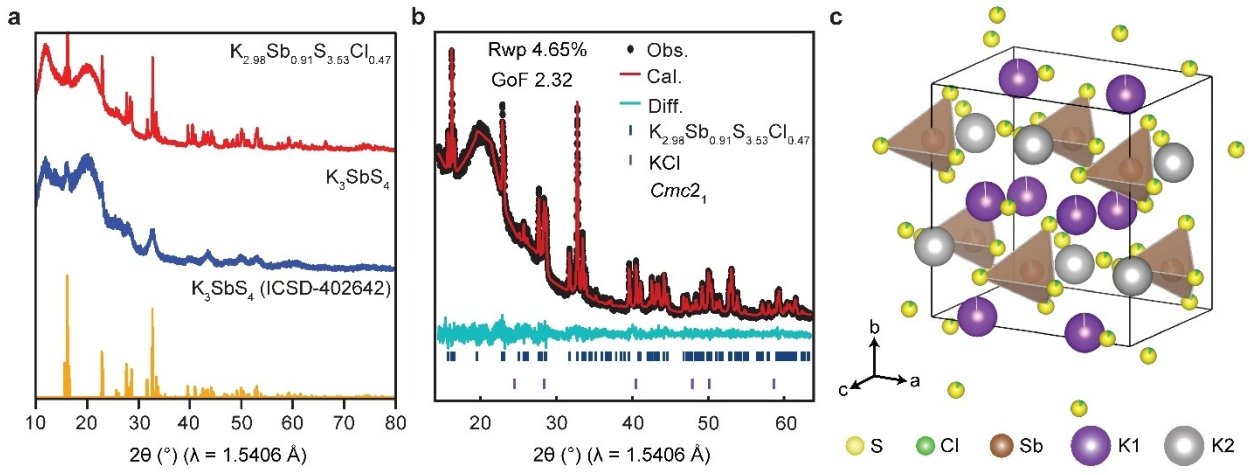

Figure 1. PXRD characterization of $K_{2.98}Sb_{0.91}S_{3.53}Cl_{0.47}$. (a) Comparison of PXRD patterns of $K_{2.98}Sb_{0.91}S_{3.53}Cl_{0.47}$, K_3SbS_4, and β-K_3SbS_4 obtained from ICSD database. (b) PXRD patterns and the corresponding Rietveld refinement of $K_{2.98}Sb_{0.91}S_{3.53}Cl_{0.47}$. (c) Crystal structure of $K_{2.98}Sb_{0.91}S_{3.53}Cl_{0.47}$ obtained from the Rietveld refinement shown in (b).

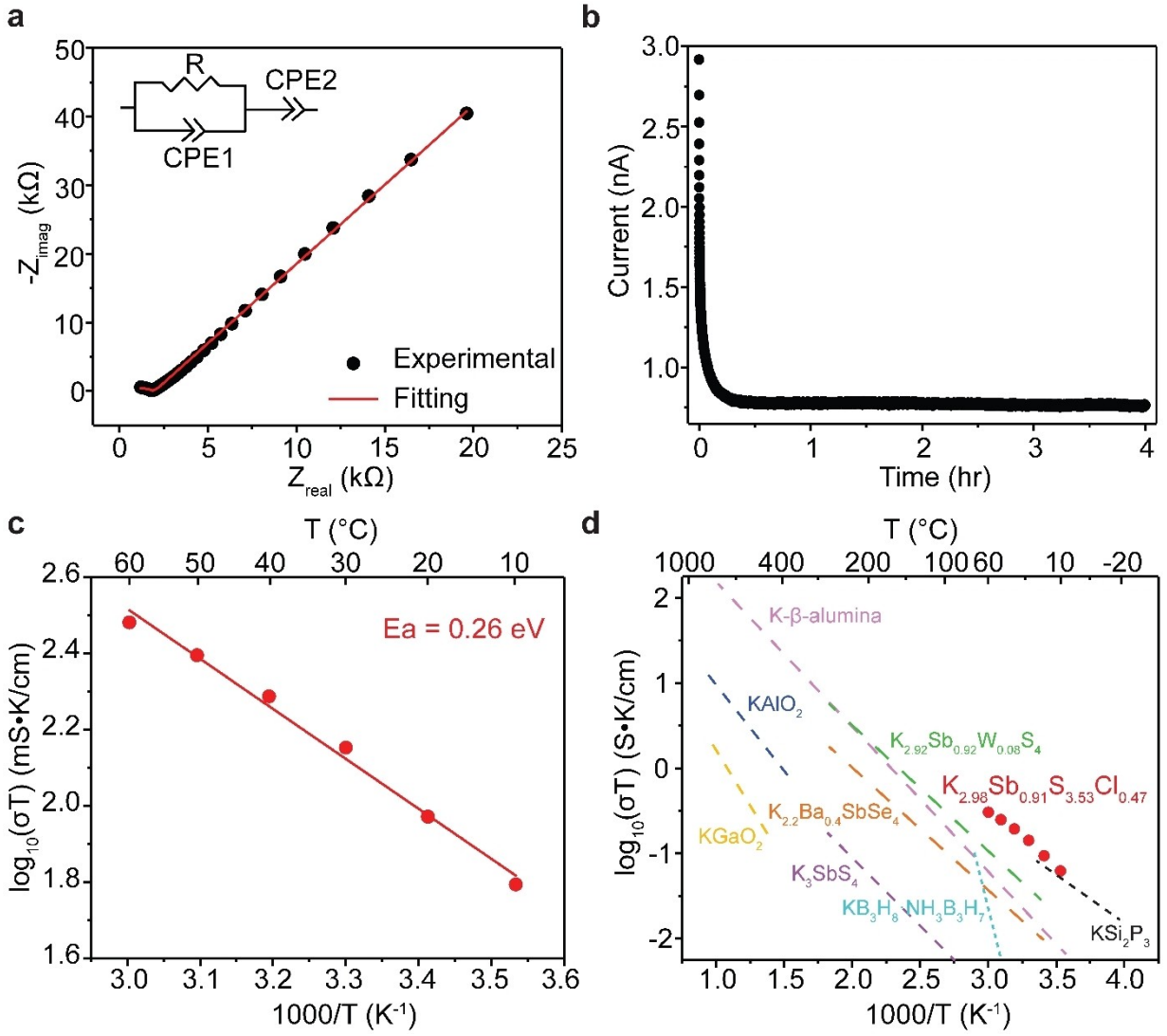

Figure 2. Ionic and electronic conductivities of $K_{2.98}Sb_{0.91}S_{3.53}Cl_{0.47}$. (a) The Nyquist plot of $K_{2.98}Sb_{0.91}S_{3.53}Cl_{0.47}$ at room temperature using AC electrochemical impedance spectroscopy with equivalent circuit fitting, yielding an ionic conductivity of 0.32 mS/cm. (b) Potentiostatic polarization curve of $K_{2.98}Sb_{0.91}S_{3.53}Cl_{0.47}$ with ion-blocking electrodes at room temperature, resulting in a low electronic conductivity of 1.5×10^{-8} S/cm. (c) The Arrhenius plot of the ionic conductivity of $K_{2.98}Sb_{0.91}S_{3.53}Cl_{0.47}$ versus temperature and the extracted activation energy. (d) Comparison of ion transport properties of $K_{2.98}Sb_{0.91}S_{3.53}Cl_{0.47}$ with other solid-state K-ion conductors.

ature. $K_{2.98}Sb_{0.91}S_{3.53}Cl_{0.47}$ exhibits an activation energy of 0.26 eV for K^+ transport. The effect of different Cl doping levels on the ionic conductivity of the material is also explored, with $K_{2.98}Sb_{0.91}S_{3.53}Cl_{0.47}$ exhibiting the highest ionic conductivity at room temperature (Figure S5).

Figure 2d provides an overview of recently discovered potassium SEs with ionic conductivities surpassing 0.1 mS/cm (see Table S3 for detailed information). Predominantly, these SEs are oxides, showcasing practical ionic conductivities only at elevated temperatures. Examples include $KAlO_2$ and $KGaO_2$, exhibiting ionic conductivities of 1 mS/cm and 0.1 mS/cm at 400 °C, respectively.[23,25] Non-oxide potassium SEs exhibit relatively high room-temperature ionic conductivities. For instance, KSi_2P_3, featuring T5 super-tetrahedra, demonstrates a room-temperature ionic conductivity of up to 0.26 mS/cm.[27] $K_{2.2}Ba_{0.4}SbSe_4$ achieves an ionic conductivity of 0.1 mS/cm at 40 °C.[36] K_3SbS_4, the parent material of $K_{2.98}Sb_{0.91}S_{3.53}Cl_{0.47}$, exhibits a low total ionic conductivity of 2.5×10^{-3} mS/cm at room temperature; the W-modified variant, $K_{2.92}Sb_{0.92}W_{0.08}S_4$, shows an improved total ionic conductivity of 7.7×10^{-2} mS/cm.[28] In this work, we discovered an anion-doped $K_{2.98}Sb_{0.91}S_{3.53}Cl_{0.47}$ with a room-temperature ionic conductivity of 0.32 mS/cm. This value exceeds two orders of magnitude compared to the parent K_3SbS_4, marking the highest reported conductivity among non-oxide-based potassium ion conductors.

To understand the effect of Cl^- doping on the K^+ local structural environment and dynamics, we employed ^{39}K (spin-3/2) magic-angle-spinning (MAS) NMR. Previous geometrical-topological analysis has predicted the K^+ diffusion network in β-K_3SbS_4, suggesting that K^+ ions predominantly migrate between adjacent K1 sites along the c-direction.[28]

As shown in Figure 3a, ^{39}K MAS NMR spectrum of the as-synthesized K_3SbS_4 reveals two distinct potassium environments manifested by a broad resonance centered at −90.0 ppm and a small sharp resonance at 45.0 ppm. The large line widths of the −90.0 ppm resonances indicate substantial quadrupolar coupling interactions, which could be attributed to low symmetry in the local environment and slow ion dynamics. It is noted that the broad resonance is fitted with two different sites. Specifically, the resonance with an isotropic shift of −14.8 ppm (Figure 3a, colored in blue) exhibits a large quadrupole coupling constant of C_Q = 2.6 MHz and quadrupolar asymmetry parameter η_Q = 0.22. This resonance is assigned to the less mobile K2 site in β-K_3SbS_4. The resonance with an isotropic shift of 19.7 ppm (Figure 3a, shown in green) and a smaller quadrupole coupling constant of C_Q = 1.3 MHz is attributed to α-K_3SbS_4, a polymorph that can potentially coexist with β-K_3SbS_4.[28] This peak assignment aligns well with the findings of the Rietveld refinement, which reveals a mixed phase consisting of 66.7 % β-K_3SbS_4 and 33.3 % α-K_3SbS_4 within the synthesized K_3SbS_4 sample (Figure S2 and Table S2). The sharp resonance with an isotropic shift of 45.0 ppm (Figure 3a, shown in orange) is assigned to the more mobile K1 site in β-K_3SbS_4. Similar peak patterns are observed in ^{23}Na NMR spectra for $NaNbO_3$ and $NaNb_{13}O_{33}$, where Na with faster local Na dynamics results in a narrower resonance.[37]

After partially replacing S^{2-} with Cl^-, the broad ^{39}K NMR resonance shifts its center of gravity to −100.0 ppm, and the sharp peak shifts to 48.2 ppm (Figure 3b), indicating changes in local K environments. The broad peak (Figure 3b, shown in blue) is fitted with one K site, with an isotropic shift of - 59.7 ppm, a large nuclear quadrupole coupling constant of C_Q = 3.2 MHz, and an asymmetry parameter η_Q = 0.15. The sharp ^{39}K resonance of $K_{2.98}Sb_{0.91}S_{3.53}Cl_{0.47}$ at 48.0 ppm exhibits a narrower line width and lower field shift than K_3SbS_4, indicating enhanced K^+ dynamics. Furthermore, the pronounced increase in the intensity of the sharp resonance suggests a notable rise in the population of the mobile K^+ at the K1 sites. The increased charge carrier concentration and high ion mobility collectively enhance ion conduction.

Raman spectroscopy is a useful technique, complementary to NMR, that can characterize the short-range structure of the materials. Figure 3b shows the Raman spectra acquired for both the as-synthesized K_3SbS_4 and the $K_{2.98}Sb_{0.91}S_{3.53}Cl_{0.47}$ samples. The observed Raman peaks resonating at around 353, 370, and 390 cm^{-1}, are attributed to the symmetric (V_s) and asymmetric (V_a) stretching vibrations associated with the SbS_4^{3-} polyanions in K_3SbS_4. The introduction of Cl to the SbS_4^{3-} polyanion results in a notable shift of the Raman peaks towards higher wavenumbers, specifically at 357, 374, and 394 cm^{-1}, indicative of a successful modification of the Sb–S bond through Cl incorporation. In Raman spectra, peak shifts are related to changes in chemical bond lengths. A decrease in bond length typically leads to a shift of Raman peaks towards higher wavelengths.[38] The unit cell of β-K_3SbS_4 is determined to be 931.7726 Å^3.[28] Following Cl doping, the volume of $K_{2.98}Sb_{0.91}S_{3.53}Cl_{0.47}$ decreases to 930.1298 Å^3 (Table S1). The volume reduction observed in XRD Rietveld refinement aligns consistently with the findings from Raman spectroscopy. A comparable shift in Raman peaks is also noted in the previously reported Cl-doped Na_3SbS_4 sample.[39]

To further understand the effect of Cl^--S^{2-} anion mixing on the K^+ density distribution and diffusion, ab initio molecular dynamics (AIMD) simulations are performed for

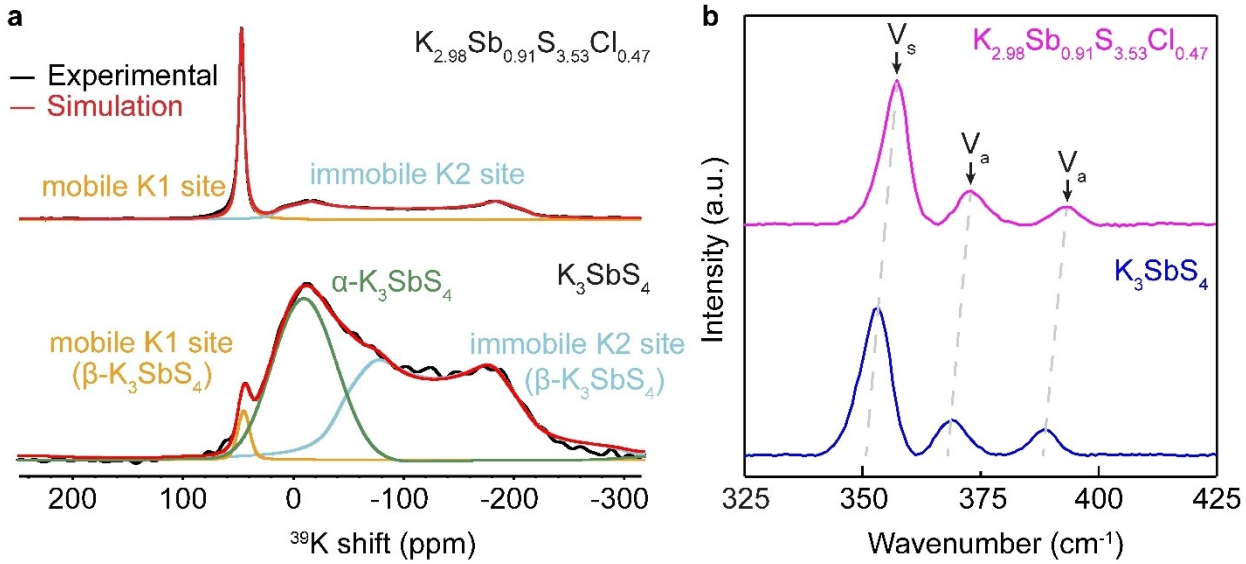

Figure 3. (a) ^{39}K MAS NMR spectra of the as-synthesized K_3SbS_4 (bottom, green lines for the α-K_3SbS_4, orange lines for the mobile K1 site in the β-K_3SbS_4, and light blue lines for the immobile K2 site in the β-K_3SbS_4) and $K_{2.98}Sb_{0.91}S_{3.53}Cl_{0.47}$ (top, orange lines for the mobile K1 site and light blue lines for the immobile K2 site), acquired at an MAS rate of 16 kHz in a magnetic field of 19.6 T. (b) Raman spectra of as-synthesized K_3SbS_4 (bottom, blue lines) and $K_{2.98}Sb_{0.91}S_{3.53}Cl_{0.47}$ (top, purple lines). V_s and V_a denote symmetric and asymmetric stretching vibrations associated with the SbS_4^{3-} polyanions, respectively.

β-K_3SbS_4 and $K_{2.98}Sb_{0.91}S_{3.53}Cl_{0.47}$ in a $1 \times 1 \times 1$ supercell respectively. Figure 4a displays the distribution probability maps for K^+ at 900 K. The AIMD simulation of K^+ trajectories in β-K_3SbS_4 shows an isolated and localized "cage-like" K^+ diffusion pattern with no interstitial jump, indicating restricted long-range K^+ migration and thereby poor K^+ conduction in β-K_3SbS_4, which is in good agreement with the experimental results that β-K_3SbS_4 has a low ionic conductivity at room temperature.[28] Unlike the undoped β-K_3SbS_4, $K_{2.98}Sb_{0.91}S_{3.53}Cl_{0.47}$ exhibits a delocalized K^+ density network, as shown in Figure 4b, suggesting improved K^+ diffusion after introducing local disorder via anion mixing. The AIMD simulation result is consistent with our experimental data, in which the ionic conductivity of $K_{2.98}Sb_{0.91}S_{3.53}Cl_{0.47}$ increases over two orders of magnitude compared with β-K_3SbS_4.

Figure 4c and Figure 4d show mean square displacements (MSD) of K^+ at 900 K for β-K_3SbS_4 and $K_{2.98}Sb_{0.91}S_{3.53}Cl_{0.47}$, respectively. Previous geometrical-topological analysis has predicted a two-dimensional K^+ diffusion network in β-K_3SbS_4.[28] However, our AIMD simulation shows that K^+ ions only have minimal diffusion in the *c* direction, and no noticeable K^+ movement is observed in the *a* and *b* directions, suggesting that β-K_3SbS_4 is a one-dimensional K^+ ion conductor. In contrast, the MSD plots for $K_{2.98}Sb_{0.91}S_{3.53}Cl_{0.47}$ show significant enhancement in K^+ diffusional movement, which is one order of magnitude higher than β-K_3SbS_4. The result demonstrates that K^+ diffusion in $K_{2.98}Sb_{0.91}S_{3.53}Cl_{0.47}$ is predominantly along the *c* direction with notable movement in the *a* and *b* directions.

Linear sweep voltammetry (LSV) is conducted to determine the electrochemical stability window of $K_{2.98}Sb_{0.91}S_{3.53}Cl_{0.47}$. The LSV measurements are carried out at room temperature to two identical cells with a configuration of K-Sn/$K_{2.98}Sb_{0.91}S_{3.53}Cl_{0.47}$ (SE)/C:SE using a scan rate of 0.2 mV/s. Carbon (super P) is utilized here as an electronic conductive medium in the composite cathode, allowing a more accurate measurement of the electro-

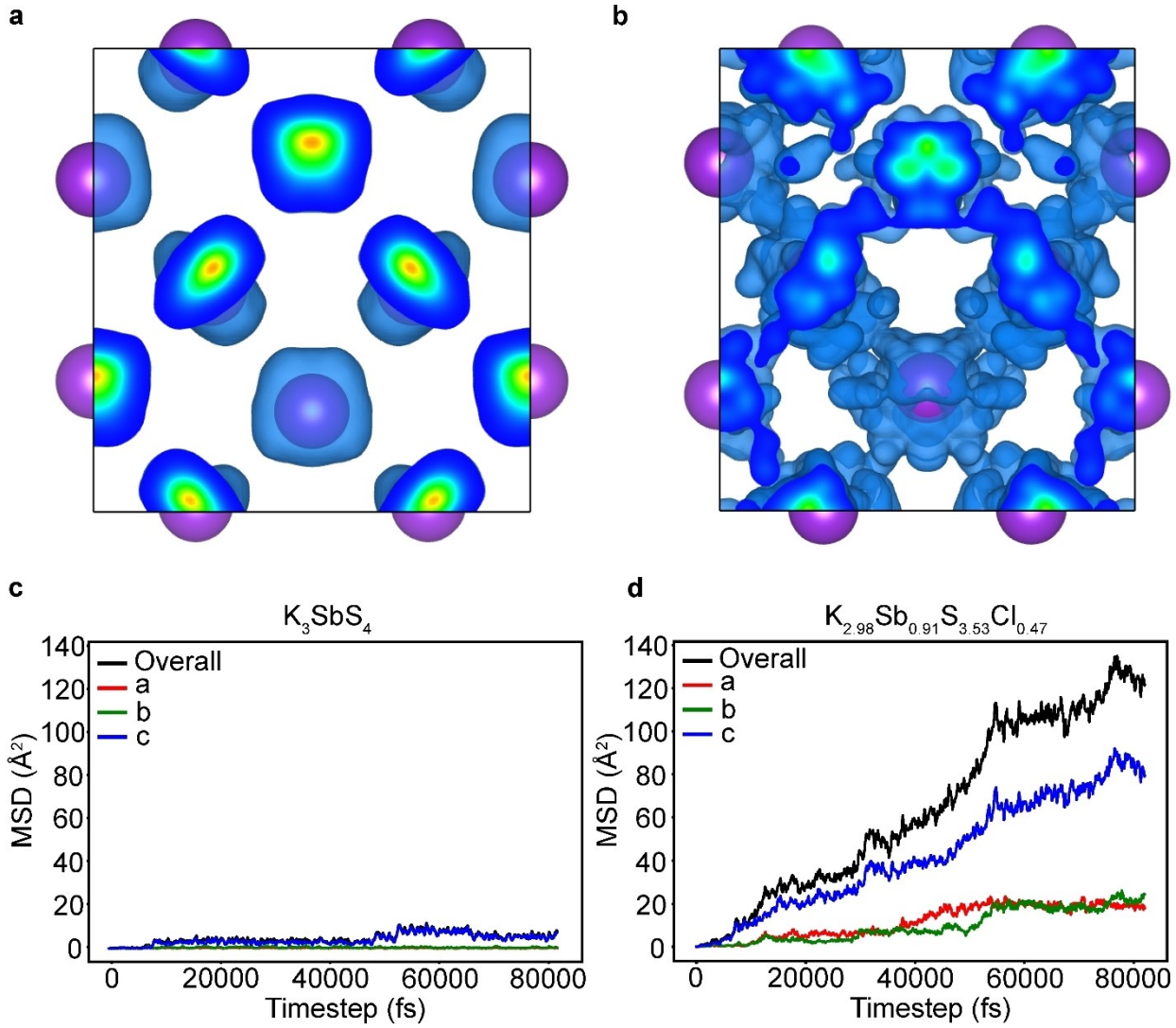

Figure 4. K^+ density distribution in (a) K_3SbS_4 and (b) $K_{2.98}Sb_{0.91}S_{3.53}Cl_{0.47}$ in a 1×1×1 cell based on AIMD simulations at 900 K. Mean square displacements (MSD) of K^+ in the (c) K_3SbS_4 and (d) $K_{2.98}Sb_{0.91}S_{3.53}Cl_{0.47}$.

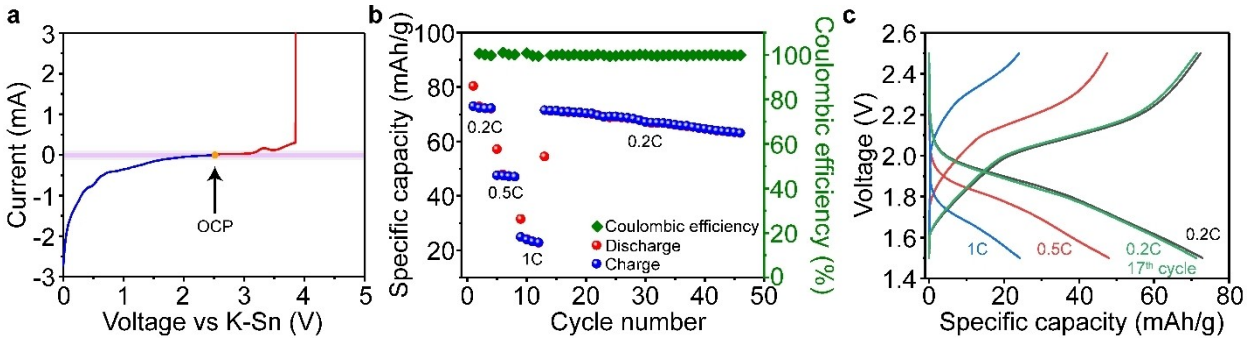

Figure 5. (a) Linear sweep voltammogram of the $K_{2.98}Sb_{0.91}S_{3.53}Cl_{0.47}$ at room temperature using a scan rate of 0.2 mV/s. (b) Rate performance cycling test for K-Sn/$K_{2.98}Sb_{0.91}S_{3.53}Cl_{0.47}$ (SE)/TiS_2:SE ASSB cell at charge and discharge rates of 0.2 C, 0.5 C, and 1 C. (c) Voltage profiles of the second cycle at each C-rate for the ASSB cells using $K_{2.98}Sb_{0.91}S_{3.53}Cl_{0.47}$.

chemical stability window due to added sensitivity in detecting degradation current. Further details on preparing the composite cathode can be found in the Supporting Information. The LSV measurements suggest that the electrochemical stability window of $K_{2.98}Sb_{0.91}S_{3.53}Cl_{0.47}$ ranges from around 1.5 to 3.2 V versus K-Sn (Figure 5a).

To evaluate the performance of $K_{2.98}Sb_{0.91}S_{3.53}Cl_{0.47}$ used in ASSBs, a battery cell with the configuration of K-Sn/$K_{2.98}Sb_{0.91}S_{3.53}Cl_{0.47}$/$TiS_2$: $K_{2.98}Sb_{0.91}S_{3.53}Cl_{0.47}$ is prepared. K-Sn alloy is the anode, $K_{2.98}Sb_{0.91}S_{3.53}Cl_{0.47}$ serves as the solid electrolyte, and a composite cathode employs TiS_2 as the cathode active material (CAM) at a loading of 1.28 mAh/cm^2. Electrochemical cycling is conducted at room temperature within a voltage window of 1.5–2.5 V, using varied charge–discharge rates, 0.2 C, 0.5 C, and 1 C, over 4 cycling loops, followed by an additional 34 cycles at 0.2 C (Figure 5b). The corresponding cycling voltage profiles for the second cycle of each C-rate are displayed in Figure 5c. The battery cell demonstrates a good average coulombic efficiency of 99.8 % and maintains 87 % of its capacity after undergoing an additional 34 cycles at a 0.2 C rate following the C rate test (Figure 5b).

Conclusion

In summary, we have successfully synthesized $K_{2.98}Sb_{0.91}S_{3.53}Cl_{0.47}$, yielding a remarkable room-temperature ionic conductivity of 0.32 mS/cm with a low activation energy of 0.26 eV. By diversifying the anion sublattice, the ionic conductivity of $K_{2.98}Sb_{0.91}S_{3.53}Cl_{0.47}$ has increased by over two orders of magnitude compared with the parent compound K_3SbS_4, marking the highest room-temperature ionic conductivity among reported non-oxide potassium ion conductors. Furthermore, $K_{2.98}Sb_{0.91}S_{3.53}Cl_{0.47}$ exhibits negligible electron conduction, affirming its predominant role as a K^+ ion conductor. The ^{39}K MAS NMR analysis reveals an increased population of mobile K^+ ions and fast K^+ dynamics, while AIMD simulations corroborate enhanced K^+ diffusion with the introduction of Cl^- into K_3SbS_4. This study demonstrates anion doping as an effective strategy to improve ion diffusion and underscores the potential of $K_{2.98}Sb_{0.91}S_{3.53}Cl_{0.47}$ as a promising SE material for all-solid-state potassium batteries. Furthermore, $K_{2.98}Sb_{0.91}S_{3.53}Cl_{0.47}$ exhibits robust capacity retention upon cycling in ASSBs when coupled with TiS_2 as the cathode material.

Acknowledgements

The authors acknowledge the support from the National Science Foundation under grant no. DMR-1847038. All solid-state NMR experiments were performed at the National HighMagnetic Field Laboratory, which is supported by National Science Foundation Cooperative Agreement Nos. DMR-1644779 and DMR-2128556 and the State of Florida.

Conflict of Interest

The authors declare no conflict of interest.

Data Availability Statement

The data that support the findings of this study are available from the corresponding author upon reasonable request.

Keywords: energy storage · ^{39}K NMR · potassium batteries · potassium ion transport · solid electrolytes

[1] J. Janek, W. G. Zeier, *Nat. Energy* **2016**, *1*, 16141.
[2] A. Manthiram, X. Yu, S. Wang, *Nat. Rev. Mater.* **2017**, *2*, 16103.
[3] T. Placke, R. Kloepsch, S. Dühnen, M. Winter, *J. Solid State Electrochem.* **2017**, *21*, 1939–1964.
[4] T. Famprikis, P. Canepa, J. A. Dawson, M. S. Islam, C. Masquelier, *Nat. Mater.* **2019**, *18*, 1278–1291.
[5] Q. Zhao, S. Stalin, C.-Z. Zhao, L. A. Archer, *Nat. Rev. Mater.* **2020**, *5*, 229–252.
[6] R. Murugan, V. Thangadurai, W. Weppner, *Angew. Chem. Int. Ed.* **2007**, *46*, 7778–7781.

[7] W. D. Richards, L. J. Miara, Y. Wang, J. C. Kim, G. Ceder, *Chem. Mater.* **2016**, *28*, 266–273.
[8] M. Nasir, J. Y. Park, P. Heo, K. H. Choi, H. J. Park, *Adv. Funct. Mater.* **2023**, *33*, 2303397.
[9] P. Wang, H. Liu, S. Patel, X. Feng, P.-H. Chien, Y. Wang, Y.-Y. Hu, *Chem. Mater.* **2020**, *32*, 3833–3840.
[10] S. V. Patel, S. Banerjee, H. Liu, P. Wang, P.-H. Chien, X. Feng, J. Liu, S. P. Ong, Y.-Y. Hu, *Chem. Mater.* **2021**, *33*, 1435–1443.
[11] P. Wang, S. Patel, H. Liu, P. Chien, X. Feng, L. Gao, B. Chen, J. Liu, Y. Hu, *Adv. Funct. Mater.* **2023**, 2307954.
[12] L. Zhou, A. Assoud, Q. Zhang, X. Wu, L. F. Nazar, *J. Am. Chem. Soc.* **2019**, *141*, 19002–19013.
[13] H. Vikström, S. Davidsson, M. Höök, *Appl. Energy* **2013**, *110*, 252–266.
[14] H. U. Sverdrup, *Resour. Conserv. Recycl.* **2016**, *114*, 112–129.
[15] Y. Liu, F. Fan, J. Wang, Y. Liu, H. Chen, K. L. Jungjohann, Y. Xu, Y. Zhu, D. Bigio, T. Zhu, C. Wang, *Nano Lett.* **2014**, *14*, 3445–3452.
[16] H. S. Hirsh, Y. Li, D. H. S. Tan, M. Zhang, E. Zhao, Y. S. Meng, *Adv. Energy Mater.* **2020**, *10*, 2001274.
[17] L. Qin, L. Schkeryantz, Y. Wu, *Angew. Chem. Int. Ed.* **2023**, *62*, e202213996.
[18] Y. Xu, M. Titirici, J. Chen, F. Cora, P. L. Cullen, J. S. Edge, K. Fan, L. Fan, J. Feng, T. Hosaka, J. Hu, W. Huang, T. I. Hyde, S. Imtiaz, F. Kang, T. Kennedy, E. J. Kim, S. Komaba, L. Lander, P. N. Le Pham, P. Liu, B. Lu, F. Meng, D. Mitlin, L. Monconduit, R. G. Palgrave, L. Qin, K. M. Ryan, G. Sankar, D. O. Scanlon, T. Shi, L. Stievano, H. R. Tinker, C. Wang, H. Wang, H. Wang, Y. Wu, D. Zhai, Q. Zhang, M. Zhou, J. Zou, *J. Phys. E* **2023**, *5*, 021502.
[19] B. L. Ellis, L. F. Nazar, *Curr. Opin. Solid State Mater. Sci.* **2012**, *16*, 168–177.
[20] C. K. Moon, H.-J. Lee, K. H. Park, H. Kwak, J. W. Heo, K. Choi, H. Yang, M.-S. Kim, S.-T. Hong, J. H. Lee, Y. S. Jung, *ACS Energy Lett.* **2018**, *3*, 2504–2512.
[21] L. Zhang, D. Zhang, K. Yang, X. Yan, L. Wang, J. Mi, B. Xu, Y. Li, *Adv. Sci.* **2016**, *3*, 1600089.
[22] A. Hayashi, N. Masuzawa, S. Yubuchi, F. Tsuji, C. Hotehama, A. Sakuda, M. Tatsumisago, *Nat. Commun.* **2019**, *10*, 5266.
[23] E. I. Burmakin, G. V. Nechaev, G. Sh Shekhtman, *Russ. J. Electrochem.* **2008**, *44*, 1386–1392.
[24] E. I. Burmakin, B. D. Antonov, G. Sh Shekhtman, *Inorg. Mater.* **2010**, *46*, 540–544.
[25] G. V. Nechaev, E. I. Burmakin, *Russ. J. Electrochem.* **2011**, *47*, 1411–1414.
[26] J.-M. Doux, L. Leguay, A. Le Gal La Salle, O. Joubert, E. Quarez, *Solid State Ionics* **2018**, *324*, 260–266.
[27] A. Haffner, A. Hatz, O. E. O. Zeman, C. Hoch, B. V. Lotsch, D. Johrendt, *Angew. Chem. Int. Ed.* **2021**, *60*, 13641–13646.
[28] J. Shao, J. Zheng, L. Qin, S. Zhang, Y. Ren, Y. Wu, *Angew. Chem. Int. Ed.* **2022**, *61*, e202200606.
[29] X. Zhang, K. C. Phuah, S. Adams, *Chem. Mater.* **2021**, *33*, 9184–9193.
[30] X. Ma, Y. Xu, *ACS Appl. Mater. Interfaces* **2022**, *14*, 2939–2948.
[31] M. Botros, J. Janek, *Science* **2022**, *378*, 1273–1274.
[32] F. Strauss, J. Lin, M. Duffiet, K. Wang, T. Zinkevich, A.-L. Hansen, S. Indris, T. Brezesinski, *ACS Materials Lett.* **2022**, *4*, 418–423.
[33] S. Li, J. Lin, M. Schaller, S. Indris, X. Zhang, T. Brezesinski, C. Nan, S. Wang, F. Strauss, *Angew. Chem. Int. Ed.* **2023**, *62*, e202314155.
[34] W. Bensch, P. Diirichen, *Z. Kristallogr. New Cryst. Struct.* **1997**, *212*, 95–96.
[35] J. T. S. Irvine, D. C. Sinclair, A. R. West, *Adv. Mater.* **1990**, *2*, 132–138.
[36] J. Shao, H. Ao, L. Qin, J. Elgin, C. E. Moore, Y. Khalifa, S. Zhang, Y. Wu, *Adv. Mater.* **2023**, 2306809.
[37] A. R. Patterson, R. Elizalde-Segovia, K. E. Wyckoff, A. Zohar, P. P. Ding, W. M. Turner, K. R. Poeppelmeier, S. R. Narayan, R. J. Clément, R. Seshadri, K. J. Griffith, *Chem. Mater.* **2023**, *35*, 6364–6373.
[38] L. Popovic, D. De Waal, J. C. A. Boeyens, *J. Raman Spectrosc.* **2005**, *36*, 2–11.
[39] H. Cao, M. Yu, L. Zhang, Z. Zhang, X. Yan, P. Li, C. Yu, *J. Mater. Sci. Technol.* **2021**, *70*, 168–175.

Manuscript received: May 6, 2024
Accepted manuscript online: June 10, 2024
Version of record online: July 22, 2024